Simultaneous Mode and Polarization Conversions Via Periodic Grating Engraved on Strip Waveguide

Eman A. Elzahaby, *Student Member, IEEE*, Ahmed M. R. Fath Elbab, and Hossam M. H. Shalaby, *Senior Member, IEEE, Senior Member, OSA*

***Abstract*—A converter that manipulates the energy exchange between two arbitrary guided modes having different mode orders and polarization states is proposed. This objective is achieved through engraving a periodic grating on a strip waveguide. Theoretical analysis, based on the coupled-mode theory, is developed to match the proposed structure. In addition, coupling analysis is addressed to provide a comprehensive view regarding the various couplings that can be achieved, including acceptable margins for perturbation designing parameters and their optimum values for each coupling. Moreover, our converter is implemented via both 3D-FDTD simulation and computational solution to examine the validity of the proposed approach and verify the coupling analysis through performing two conversions, namely TM_1-to-TE_0 and TM_1-to-TE_3. The first conversion is obtained with an insertion loss of -1 dB and a crosstalk lower than -17.5 dB at a conversion length of $9.15\ \mu$m. The second is executed with an insertion loss of -1.5 dB and a crosstalk lower than -15 dB at a conversion length of $16.937\ \mu$m. Furthermore, tolerance fabrication analysis is implemented to confirm the degree of stability that the proposed structure can achieve. Finally, the findings reveal that the proposed design achieved its function at a compact length and without being restricted by the hybridization approach.**

***Index Terms*—Bragg grating, coupled-mode theory, integrated optics devices, mode chart, mode-division multiplexers, optical converters, polarization-division multiplexers, polarization rotators, silicon-on-insulator.**

I. Introduction

SILICON-ON-INSULATOR (SOI) is one of the most promising silicon platforms utilized to develop integrated photonics devices in the field of optical communications and sensing applications [1], [2]. In addition, it is compatible with well-established complementary metal-oxide-semiconductor (CMOS) fabrication technology. This allows the integration of both photonics and electronics devices on the same chip [3]. The high refractive index contrast between Si and SiO_2, and cross-sectional geometry can support multi-guided modes with polarization diversity. By manipulating those guided modes and exploiting their orthogonality feature, advanced photonics multiplexing technologies can be utilized, such as mode-division multiplexing (MDM) and polarization-division multiplexing (PDM) [4]. Accordingly, scalability is significantly upgraded.

In general, the ability to convert a given mode to the desired mode can be classified into two main types: mode converter (MC) [5]–[10] and polarization rotator (PR) [11], [12]. At the same time, the earlier conversion among modes with different mode orders is performed without switching the polarization type, whereas the latter switches the polarization for similar mode orders. Hence, the main purpose of this work is to simultaneously manipulate mode order and polarization state using a single device rather than combining the previously reported MC and PR. Interestingly, few prior studies have investigated this area [13]–[15]. However, they are inadequate due to some limitations in their methods, as will be discussed later.

Converter devices are mainly based on three approaches. One conversion approach depends on a gradual modulated refractive index, such as tapers and directional couplers, and thus a gradual variation is applied to the field of a given mode while propagating until being transformed into the desired mode. Therefore, these structures usually have a large footprint. Dai *et al.* examined the conversion between TM_0 and TE_3 modes based on regular lateral tapers, where mode hybridization was observed in the modal chart [13]. Although the tapper structure exhibited well-functionality, the device was $750\ \mu$m long to reach the insertion loss (IL) of -1.5 dB dB. Another example by Dai *et al.* was performed by switching TM_0 to TE_1 of $80\ \mu$m length and IL of -1 dB. The same converter occurred at double length with similar IL when modifying the tapering region to be bilateral. It is known that using long devices results in non-uniformity challenges in the waveguide thickness, which causes a significant harmful effect on the performance [3]. Furthermore, Dai and Hao have used air as a cladding layer to convert TM_0 into TE_1 at a length of $15\ \mu$m with IL of almost -1 dB using the same hybridization approach [14]. Nonetheless, it is important to note that using air as a cladding layer is impractical to implement photonic integrated circuits.

Another conversion approach utilizes a strongly modulated refractive index structure, such as photonic crystals, plasmonics, and deeply etched trenches. Here, the intense effect on the given

Manuscript received May 21, 2021; revised July 24, 2021, September 2, 2021, and September 16, 2021; accepted September 17, 2021. Date of publication September 24, 2021; date of current version December 2, 2021. This work was supported by the Ministry of Higher Education and Scientific Research of Egypt. *(Corresponding author: Eman A. Elzahaby.)*

Eman A. Elzahaby is with the Department of Electronics and Communications Engineering, Egypt-Japan University of Science and Technology (E-JUST), 21934 Alexandria, Egypt, and also with the Department of Engineering Mathematics and Physics, Alexandria University, 21544 Alexandria, Egypt (e-mail: eman@alexu.edu.eg).

Ahmed M. R. Fath Elbab is with the Department of Mechatronics and Robotics, Egypt-Japan University of Science and Technology (E-JUST), 21934 Alexandria, Egypt (e-mail: ahmed.rashad@ejust.edu.eg).

Hossam M. H. Shalaby is with the Electrical Engineering Department, Alexandria University, 21544 Alexandria, Egypt (e-mail: shalaby@ieee.org).

Color versions of one or more figures in this article are available at https://doi.org/10.1109/JLT.2021.3115410.

Digital Object Identifier 10.1109/JLT.2021.3115410

modes produces ultra-compact devices. For instance, Cheng *et al.* designed a hybrid plasmonic tapering waveguide to convert TE_0 into TM_1 with only $11\,\mu$m device length and high IL of -4.1 dB [15]. The plasmonic effect was obtained by adding an extra golden layer. Unfortunately, this is inconsistent with CMOS fabrication technology [16].

The third typical approach is based on grating structures, such as long-period grating and Bragg grating (BG) [8]–[10], [17]. Here, the refractive indices are modulated periodically to match the phase difference between given and desired modes, and to maximize the associated field overlap. Although periodic structures were used to design MCs [8]–[10] and PRs [12], they did not achieve both functions simultaneously.

It is noteworthy that decreasing the device length is accompanied by constructing impractical and inconvenient devices, such as using air cladding medium [14] or adding extra noble material (gold layer) [15]. On the contrary, when simplifying the fabrication process, the privilege of compactness cannot be obtained [13]. Furthermore, the hybridization approach promotes specific combinations of conversions at specific widths, and any deviation in these widths causes the device to lose functionality. In order to solve this dilemma, an elite periodic structure composed of Bragg grating engraved on a strip waveguide has been proposed. By controlling the grating parameters, (e.g., its obliquity, duty cycle, and etching depth), promising coupling efficiencies can be achieved, between modes having different mode orders and polarization states in a single device.

In [18], [19], the features of this tilted structure were thoroughly examined by analyzing the coupling between modes having the same polarization states. The remarkable performance was the main impetus to expand the couplings to cover modes having different mode order and polarization states. First, a theoretical analysis is developed, based on coupled-mode theory to illustrate the working principle of the proposed conversion. This is followed by a comprehensive numerical analysis to show the versatile scope of the proposed structure, while keeping it compact and simple. Moreover, the proposed structure is verified by simulating two examples of converters, TM_1-to-TE_0 and TM_1-to-TE_3 via 3D-FDTD (from Lumerical Inc.). Additionally, these results are confirmed by solving the coupled-mode equations computationally using MATLAB. Finally, performance response of the TM_1-to-TE_3 converter is analyzed with regard to errors that may occur during fabrication. It is found that the proposed converter reveals an acceptable level of stable performance.

The remainder of the paper is organized as follows: The proposed structure is illustrated in Section II. The theoretical analysis is described in Section III. Section IV is divided into three subsections. The first subsection provides coupling analysis to demonstrate the effect of grating designing parameters on the conversion process and extract its optimum values that acquire the functionality efficiently. The second subsection addresses the spectral response obtained via both 3D-FDTD simulation and computational solution. A comparison with other reported work on some performance measures, e.g., insertion loss, crosstalk and device length, is also presented in this part. The third subsection develops an additional analysis to evaluate the tolerance of the proposed device with regard to fabrication errors. Finally, the concluding remarks are discussed in Section V.

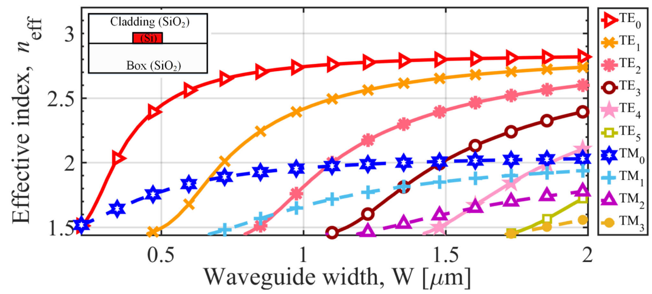

Fig. 1. Effective indices for the guided modes of a silicon strip waveguide surrounded by a silicon dioxide as a function of the waveguide width.

II. Proposed Structure

In this section, the hybridization concept is discussed to explain its weakness point. Subsequently, the proposed structure and its properties are illustrated.

The proposed SOI-based strip waveguide consists of a silicon (Si) layer of thickness $h = 220$ nm, width $W = 1.5\,\mu$m, and refractive index $n_1 = 3.475$, placed on buried oxide (SiO_2) layer of thickness $3\,\mu$m and a cladding with silicon-dioxide (SiO_2) layer of thickness $2\,\mu$m, both layers have a refractive index of $n_2 = 1.444$. Using a finite-element method (FEM) mode solver (from Lumerical Inc.), the number of supported guided modes is eight modes: five TE and three TM modes. It must be noted that the guided modes are not pure TE or TM polarized anymore, due to lateral and vertical confinements. To be more precise, the guided modes are TE- or TM-quasi, depending on whether they are predominantly polarized in y or z direction. For the sake of simplicity, TE- and TM-quasi modes will be denoted as TE and TM modes, respectively.

Fig. 1 exhibits the effective indices for the guided modes as a function of core width within a range of 0.2 to $2\,\mu$m. It is evident that polarization discrepancy strongly appears. At specific widths, mode hybridization occurs where the refractive indices of TE and TM modes become equal. In [13]–[15], mode hybridization was used as a simple approach to switch the polarization state. However, it is obvious that limited conversion cases can be obtained in addition to the obstacles illustrated in Section I.

To overcome the limitation of the hybridization approach, a periodic structure is introduced in which coupling among any two arbitrary modes, having different mode orders and polarization states, becomes feasible. Due to the orthogonality feature between TE and TM modes, the symmetry should be broken along one or both transverse axes, y and z. As shown in Fig. 2, we utilize a partially etched periodic grating of depth d, period Λ, and duty cycle τ, which indicates the percentage between the widths of Si and SiO_2 partitions in a single period. The grating planes are tilted in the clockwise direction (with respect to y-axis) by an angle. The total perturbed region is $L = N_g\Lambda + W\tan(\theta)$, where N_g is the number of periods. When the light is launched to the input port propagating in the

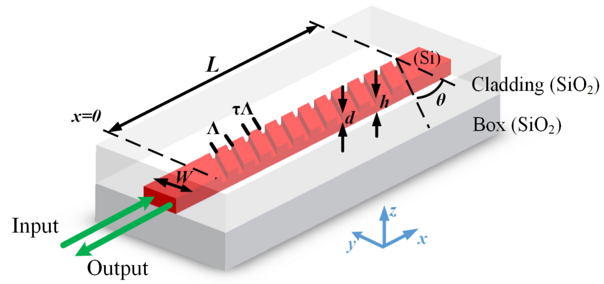

Fig. 2. Schematic structure of the proposed converter based on a Bragg grating engraved on an SOI strip waveguide.

forward direction, the output is reflected at the same input port as shown in Fig. 2. Therefore, circulators [20] are required to drop the reflected light, but they are incompatible with CMOS technology, as they are constructed from magnetic materials. Directional couplers [10] and contra-directional grating couplers [21] offer appropriate solutions by dropping the reflected mode at another waveguide to avoid backscattering effect. These solutions are consistent with CMOS fabrication technology.

By adopting the perturbation approach, the refractive index of the proposed converter can be expressed as:

$$n^2(x,y,z) = n^2_{\text{waveguide}}(y,z) + \Delta n^2_{\text{grating}}(x,y,z), \qquad (1)$$

where, $n_{\text{waveguide}}(y,z)$ and $n_{\text{grating}}(x,y,z)$ are the refractive indices of the unperturbed strip waveguide and the Bragg grating, respectively. The refractive index for the unperturbed waveguide is written as:

$$n^2_{\text{waveguide}}(y,z) = \begin{cases} n_1^2; & |y| \le w/2, 0 \le z \le h, \\ n_2^2; & \text{otherwise.} \end{cases} \qquad (2)$$

Considering that $L \gg \Lambda$, the refractive index of periodic Bragg grating perturbation using the Fourier series can be expanded as follows:

$$\Delta n^2_{\text{grating}}(x,y,z) = \begin{cases} \sum_{\nu=-\infty}^{\infty} b_\nu e^{\frac{-j2\pi(1-\tau)}{\Lambda}(x\cos(\theta)-y\sin(\theta))}; \\ \qquad |y| \le \frac{w}{2}, h-d < z \le h, \\ 0; \qquad \text{otherwise,} \end{cases} \qquad (3)$$

where, b_ν is the ν^{th} Fourier coefficient, given by:

$$b_\nu = \left(n_1^2 - n_2^2\right)(1-\tau)\,\text{sinc}\left(\nu(1-\tau)\right), \quad \nu \in \{\dots,-1,0,1,\dots\}. \qquad (4)$$

III. Theoretical Analysis

In this section, the coupled-mode theory (CMT) [17], [22], [23] is reformulated to predict the coupling and interference of optical guided modes in the presence of proposed perturbation in (3).

When a given mode is launched into a strip waveguide, its field and propagation constant are affected by the periodic perturbation. Accordingly, the perturbed field profile can be written as a superposition of all the possible supported guided modes propagating in forward and backward directions:

$$\begin{aligned} E = &\sum_{m=0}^{\mathcal{N}} \mathcal{A}_m^{\text{TE}}(x)\mathcal{E}_m^{\text{TE}}(y,z)e^{-j\beta_m^{\text{TE}}x} + \mathcal{B}_m^{\text{TE}}(x)\mathcal{E}_m^{\text{TE}}(y,z)e^{+j\beta_m^{\text{TE}}x} \\ &+ \sum_{m'=0}^{\mathcal{N}'} \mathcal{A}_{m'}^{\text{TM}}(x)\mathcal{E}_{m'}^{\text{TM}}(y,z)e^{-j\beta_{m'}^{\text{TM}}x} \\ &+ \mathcal{B}_{m'}^{\text{TM}}(x)\mathcal{E}_{m'}^{\text{TM}}(y,z)e^{+j\beta_{m'}^{\text{TM}}x}. \end{aligned} \qquad (5)$$

Here $\mathcal{N}$ and $\mathcal{N}'$ denote number of the guided TE and TM modes, respectively, and $m \in \{0,1,\dots,\mathcal{N}\}$ and $m' \in \{0,1,\dots,\mathcal{N}'\}$ denote the TE and TM mode order, respectively. $\mathcal{A}_m^{\text{TE}}(x)$ and $\mathcal{A}_{m'}^{\text{TM}}(x)$ are the x-dependent complex amplitudes of codirectional electric fields for modes m and m', respectively. $\mathcal{B}_m^{\text{TE}}(x)$ and $\mathcal{B}_{m'}^{\text{TM}}(x)$ are the x-dependent complex amplitudes of contra-directional electric fields for modes m and m', respectively. $\mathcal{E}(y,z)$ denotes the electric field profile, $\beta = 2\pi n_{\text{eff}}/\lambda_0$ is the corresponding propagation constant, λ_0 is the operational wavelength, and n_{eff} is the effective index of the distinguished guided mode propagating in unperturbed strip waveguide of width W. The field profiles and corresponding effective indices are calculated using FEM to extract each mode's field components, E_x, E_y, and E_z, respectively.

Traditional analysis is applied to describe the coupling due to periodic perturbation [22]–[25], by restating the coupled-mode equations for tilted engraved grating (considering Fourier coefficients for $\nu \in \{0,1\}$), as follows

$$\begin{aligned} \frac{d\mathcal{A}_n^{\text{P}}}{dx} &= j\mathcal{A}_n^{\text{P}}(x)\boldsymbol{l}_{n,n}^{\text{P,P}} + j\sum_{m}^{\mathcal{N}} \mathcal{B}_m^{\text{TE}}(x)e^{j\left(\delta_{m,n}^{\text{TE,P}}\right)x}\kappa_{m,n}^{\text{TE,P}} \\ &\quad + j\sum_{m'}^{\mathcal{N}'} \mathcal{B}_{m'}^{\text{TM}}(x)e^{j\left(\delta_{m',n}^{\text{TM,P}}\right)x}\kappa_{m,'n}^{\text{TM,P}} \\ \sum_{m=0}^{\mathcal{N}} \frac{\mathcal{B}_m^{\text{TE}}(x)}{dx} &= -j\mathcal{A}_n^{\text{P}}(x)e^{-j\left(\delta_{m,n}^{\text{TE,P}}\right)x}\kappa_{m,n}^{\text{TE,P}} - j\mathcal{B}_m^{\text{TE}}(x)\boldsymbol{l}_{m,m}^{\text{TE,TE}} \\ \sum_{m'=0}^{\mathcal{N}'} \frac{\mathcal{B}_{m'}^{\text{TM}}(x)}{dx} &= -j\mathcal{A}_n^{\text{P}}(x)e^{-j\left(\delta_{m,'n}^{\text{TM,P}}\right)x}\kappa_{m,'n}^{\text{TM,P}} \\ &\quad - j\mathcal{B}_{m'}^{\text{TM}}(x)\boldsymbol{l}_{m,'m'}^{\text{TM,TM}}, \end{aligned} \qquad (6)$$

where for any $r \in \{m, m'\}$,

$$\delta_{r,n}^{\text{P,P}} = \beta_r^{\text{P}} + \beta_n^{P} - \frac{2\pi}{\Lambda}, \qquad (7)$$

Here, the P notation indicates either TE or TM-polarized mode, while κ and $\boldsymbol{l}$ are the coupling coefficient and self-coupling components, respectively. It should be noted that the wavelength at which $\delta_{r,n}^{\text{TE,TM}}$ equals zero, is the Bragg reflection wavelength for coupling between modes that have different mode orders and polarization states.

The coupling coefficient κ indicates the overlap between fields of given and desired modes in the presence of a perturbation effect. It is expressed as follow:

$$\kappa_{n,r}^{\mathrm{TM,P}} = \frac{\pi(n_1^2-n_2^2)e^{j\pi(1-\tau)}(1-\tau)\,\mathrm{sinc}\,(1-\tau)}{\lambda n_{\mathrm{eff}_n^{TM}}\xi_n^P}\int_{-w/2}^{w/2}\int_{h-d}^{h} \times e^{+j\frac{2\pi y\tan(\theta)}{\Lambda}}\Big(E_{xn}^{\mathrm{TM}}(y,z)[E_{xr}^{p}(y,z)]^{*} + E_{yn}^{\mathrm{TM}}(y,z)[E_{yr}^{p}(y,z)]^{*} + E_{zn}^{\mathrm{TM}}(y,z)[E_{zr}^{p}(y,z)]^{*}\Big)\mathrm{d}y\,\mathrm{d}z, \tag{8}$$

Where $\xi^{\mathrm{P}} = \int_{-\infty}^{\infty}\int_{-\infty}^{\infty}\mathcal{E}_n^{\mathrm{P}}(y,z)\cdot[\mathcal{E}_n^{p}(y,z)]^{*}\mathrm{d}y\,\mathrm{d}z$ is the normalized factor, which corresponds to a power flow of one Watt per unit width in y-z plane of each mode.

The self-coupling component $\boldsymbol{l}$ gives a rise to an induced shift in the propagation constant of a mode n, and its effect is shown in shifting the Bragg wavelength. That term must be compensated while selecting the grating period to keep the Bragg resonance at 1550 nm. It is calculated as:

$$\boldsymbol{l}_{n,n}^{\mathrm{P,P}} = \frac{\pi(n_1^2-n_2^2)(1-\tau)}{\lambda n_{\mathrm{eff}_n^{p}}\xi_n^P}\int_{-w/2}^{w/2}\int_{h-d}^{h}\Big(E_{xn}^{p}(y,z)[E_{xn}^{p}(y,z)]^{*} + E_{yn}^{p}(y,z)[E_{yn}^{p}(y,z)]^{*} + E_{zn}^{p}(y,z)[E_{zn}^{p}(y,z)]^{*}\Big)\mathrm{d}y\,\mathrm{d}z. \tag{9}$$

It should be noted that there are two main complementary factors for manipulating the conversion process, the coupling coefficient, and phase matching condition. While the earlier factor is pointed out to the coupling strength, the latter is responsible for deciding whether coupling is present or no.

IV. Numerical Results and FDTD Simulations

This section starts by studying the coupling coefficients as functions of grating parameters, including tilt angle θ, duty cycle τ, and etching depth d. After identifying the optimum designing parameters, the performance of two different converters is simulated using 3D-FDTD (from Lumerical Inc.), in order to examine the validity of the current proposed concept and to show its superiority compared to previously reported work. Then, the simulated results and coupling analysis are verified by computationally calculating the spectral responses through which coupled-mode equations are solved via MATLAB. Finally, the stability of the proposed converter is tested by observing its spectral response in the presence of tolerance errors in dimensions that may occur during fabrication.

A. Coupling Analysis

We used a grating with an etching depth about one-half of strip thickness ($d = 110$ nm), a duty cycle of 0.85, and a period of 400 nm. The selection of these values will be explained later. The coupling coefficients, given by (8), are calculated for any two

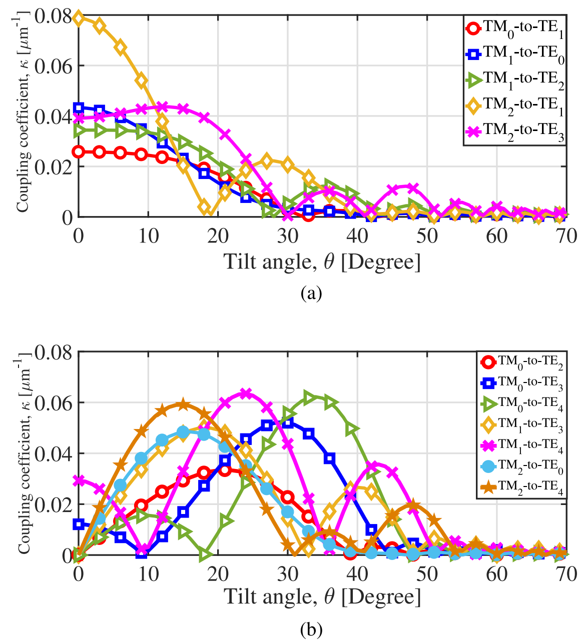

Fig. 3. Coupling coefficient as a function of the grating tilt angle of a given n and a desired m modes, having different polarization states for: (a) $|m-n| = 1$; (b) $|m-n| \geq 2$.

arbitrary modes having different mode orders and polarization states. The results are plotted in Fig. 3 for different grating tilt angles (ranging from 0° to 70°).

As shown, each curve has multiple peaks and nulls due to the impact of field overlapping between the coupled modes in the presence of periodic Bragg perturbation presented in terms of exponential form, as described in (3). A unique global maximum coupling value exists at an optimum tilt angle θ_{opt} for each curve. In fact, the possible couplings are divided according to the difference in mode orders between given mode m and desired mode n: If $|m-n| = 1$, then the global maximum coupling coefficient occurs at $\theta_{\mathrm{opt}} = 0^\circ$, whereas for the coupled modes with $|m-n| \geq 2$, the global maximum coupling coefficient appears at $\theta_{\mathrm{opt}} > 0$. For instance, as shown in Figs. 3(a) and 3(b), θ_{opt} are equal to 0° and 18° for TM_1-to-TE_0 and TM_1-to-TE_3 couplings, respectively. These findings will be further explained later in the following discussion.

Since the coupling coefficient is calculated by summing three dot products related to three electric field components, as expressed in (8), the electric field components for TE_0, TM_1, and TE_3 modes are plotted in Fig. 4, to explain TM_1-to-TE_0 and TM_1-to-TE_3 couplings. The dot product of E_z can be ignored, as it causes a minor effect on the coupling coefficients for each conversion. Focusing on the E_y and E_x components, it is required to manipulate the field distributions of the given mode TM_1 to increase their dot products with corresponding components of the desired mode TE_0. Consequently, the coupling coefficient is maximized. Along z-axis, it is observed that the components of the given mode show anti-symmetrical distributions and have opposite signs compared with to those of the desired mode. So it is required to break the structure symmetry via partially etching the upper part of the strip waveguide to make the distribution of the given components symmetrical along with z-axis. When

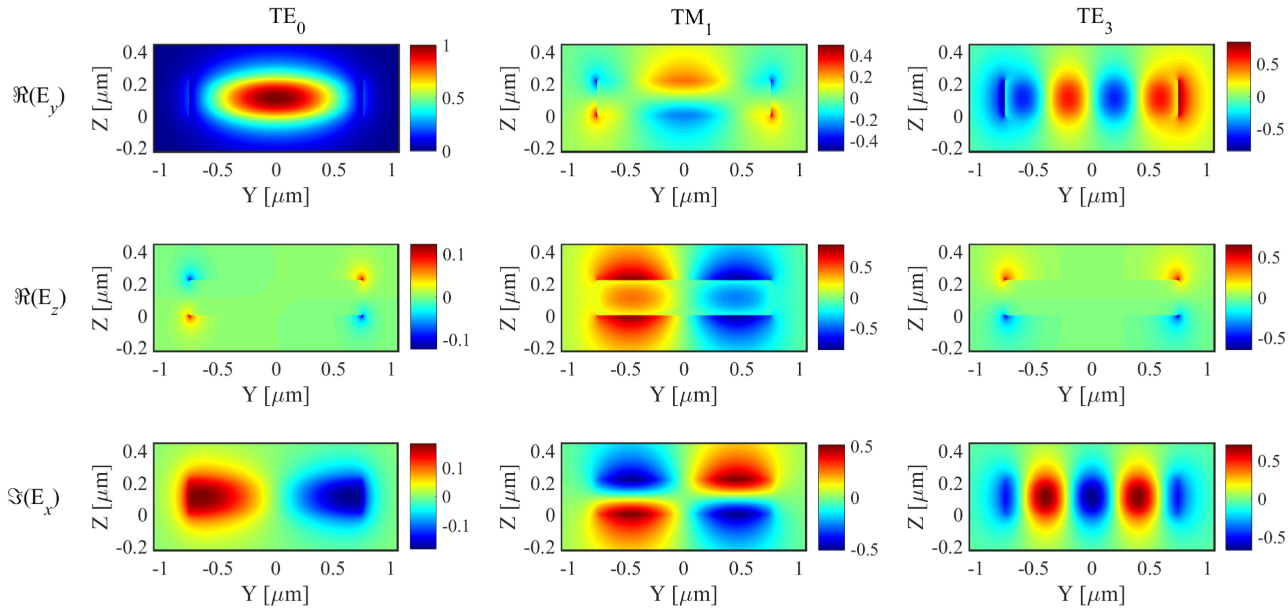

Fig. 4. The electric field profiles are displayed for TE_0 (first column), TM_1 (second column) and TE_3 (third column).

applying dot products in the presence of the etching region, both $E_y^{\mathrm{TM}_1} \cdot [E_y^{\mathrm{TE}_0}]^*$ and $E_x^{\mathrm{TM}_1} \cdot [E_x^{\mathrm{TE}_0}]^*$ have similar sign; hence, their the resultant summation is maximized.

Interestingly, there is no need to add perturbation along the y-axis, because the field components of both given and desired modes are symmetrically distributed to each other in the presence of perturbation along z-axis. In contrast, when the desired mode is TE_3, the corresponding field components show a high degree of contrast compared with the given mode TM_1, and to achieve the maximum resultant summation of corresponding dot products, the symmetry must be broken partially in z-axis and diagonally in y-axis.

Conventionally, when dealing with coupling among modes that have different polarization states, breaking the symmetry in the transverse directions (y and z) is required. This deduction reasonably agrees with the designing concept reported in [12] for the fundamental-mode PR with anti-symmetrical grating.

In a related context, the coupling coefficients are examined as a function of grating duty cycle and etching depth, as they affect the perturbation strength. A simple approach is introduced to figure out the appropriate ranges of grating duty cycle and etching depth that efficiently perform within the Bragg grating region.

First, the average value of the core refractive index of the proposed structure is calculated as a function of both grating duty cycle and etching depth [17], through the following equation:

$$n_{\mathrm{av}} = \sqrt{\left(\frac{h-d}{h}\right) n_1^2 + \frac{d}{h}\left[\tau n_1^2 + (1-\tau) n_2^2\right]}. \qquad (10)$$

Subsequently, the propagation characteristics, including the effective refractive indices and their associated fields, for the guided modes are determined, considering a strip waveguide having a core refractive index of n_{av}, as expressed in (10), instead of n_1. Changing the grating duty cycle or etching depth affects the coupling coefficient values calculated at θ_{opt} for each case, as illustrated in Fig. 5.

It is pointed out that if the mode order of either the given or desired mode increases, the acceptable ranges of grating duty cycle and etching depth (where the coupling coefficient has a non-zero value) become narrow. Since the average core refractive index decreases due to reducing the grating duty cycle and increasing the etching depth. Accordingly, higher modes are no longer supported. For instance, the grating duty cycle should not be less than 0.75 at an etching depth of 110 nm for TM_2-to-TE_4 conversion, while the duty cycle has a broader range of validity (greater than 0.2) for TM_0-to-TE_1 conversion at the same etching depth. In Fig. 3, a duty cycle of 0.85 is selected as a compromised value to show all cases of couplings.

Additionally, it is observed that there is a single maximum coupling coefficient for each case along with the change of the grating duty cycle or etching depth, as shown in Fig. 5. According to (8), the dependency relation between coupling coefficient and grating duty cycles is in the form of a sinc function. When increasing the grating etching depth, the coupling coefficients accumulate progressively to the optimum breaking symmetry depth of 110 nm. This is because the field distributions have only a single peak along z-axis centered at half waveguide thickness, as shown in Fig. 4.

Within the framework of optimizing grating duty cycle and etching depth of Bragg-based devices, this conclusion is consistent with the findings of [26] in which Giuntoni *et al.* measured the appropriate ranges of grating duty cycle and etching depth of Bragg reflector filter, focusing on the fundamental mode propagating through a rib-silicon waveguide.

B. Simulation Results

In this section, the performance of the proposed structure is evaluated by determining the insertion loss (IL), crosstalk (CT)

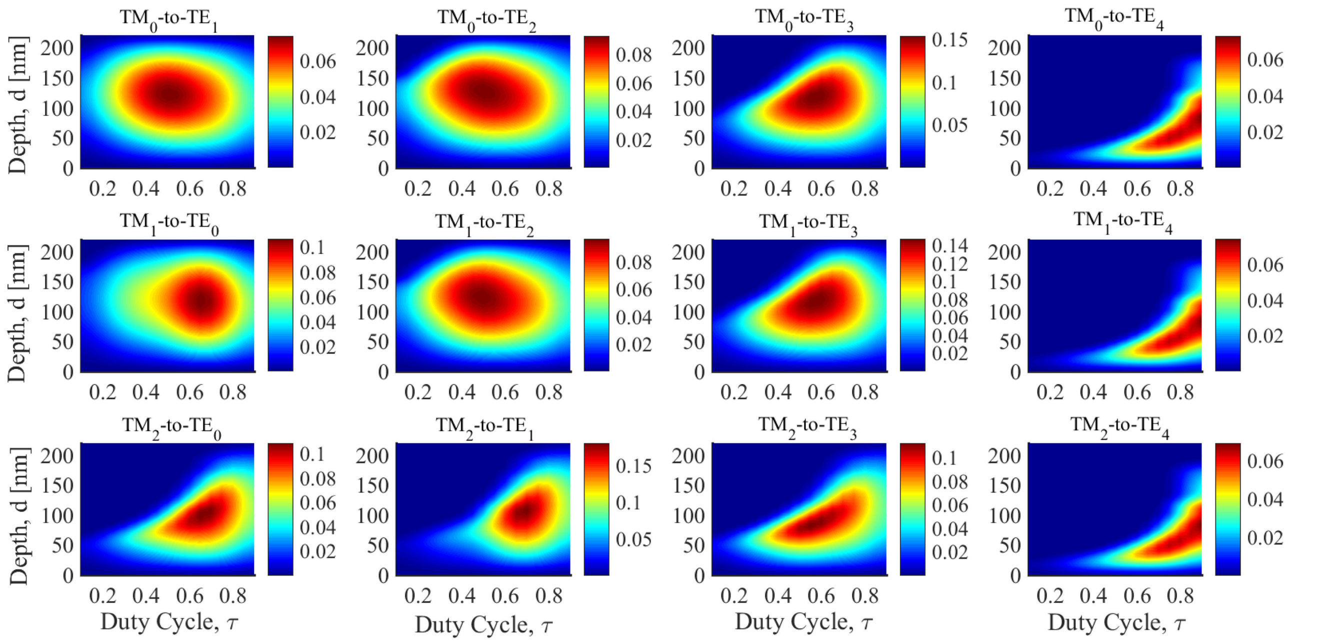

Fig. 5. Contour plot of coupling coefficient as a function of grating duty cycle and etching depth for different modes having dissimilar mode orders and polarization states.

TABLE I
GRATING DESIGNING PARAMETERS FOR DIFFERENT CONVERSION CASES

Converter	Λ [nm]	θ [Degree]	τ	d [nm]	N_g
TM$_1$-to-TE$_0$	365	0	0.7	110	25
TM$_1$-to-TE$_3$	470	18	0.65	110	35

and device length (L), then compared to the reported conversions in previous research activities [13] and [15]. The IL is the power ratio between the desired and given modes, which estimates the energy loss across the converter, while the CT measures the mode purity and is defined as the ratio between maximum interfering and desired modes. Two different converters are designed, namely; TM$_1$-to-TE$_0$ and TM$_1$-to-TE$_3$, in which their performances are shown in Fig. 6 using both 3D-FDTD simulation and computational method. These conversion cases are chosen because the high contrast between effective indices of the coupled modes prevents hybridization from occurring at $W = 1.5\,\mu$m, as shown in Fig. 1. Consequently, it is suitable to demonstrate the potential of the proposed structure.

First, the grating period for each case is obtained by satisfying the phase-matching condition in (7) between the given and desired modes. Subsequently, the optimum grating parameters are determined as discussed in Se. IV-A. Then, the spectral response is determined via two methods, 3D-FDTD simulation and computational solution, by solving the coupled-mode equations given by (6) via MATLAB. The whole designing parameters of the proposed converters are listed in Table I. The shortest distance between two adjacent silicon structures in the grating are 109.5 nm and 164.5 nm for TM$_1$-to-TE$_0$ and TM$_1$-to-TE$_3$, respectively.

These sizes are larger than the minimum resolution of the Electron-Beam Lithography, which was 50 nm as reported in [27], when fabricating a device based on a grating structure.

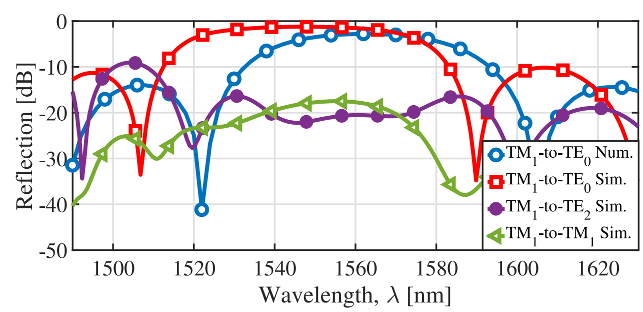

(a)

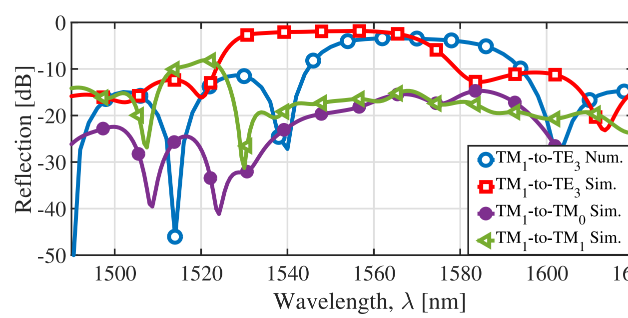

(b)

Fig. 6. FDTD simulations of insertion loss and crosstalks versus wavelength for: (a) TM$_1$-to-TE$_0$ and (b) TM$_1$-to-TE$_3$ converter devices.

Fig. 6(a) shows the results for the TM$_1$-to-TE$_0$ converter. It is clear that the IL and maximum CT are -1 dB and -17.5 dB, respectively, over a 50 nm bandwidth (from 1520 to 1570 nm). Propagation length is $L = 9.125\,\mu$m. Compared to what has been reported in [15], a length slightly shorter than theirs is achieved without adding extra material (gold layer) and without being restricted to the hybridization approach. In addition,

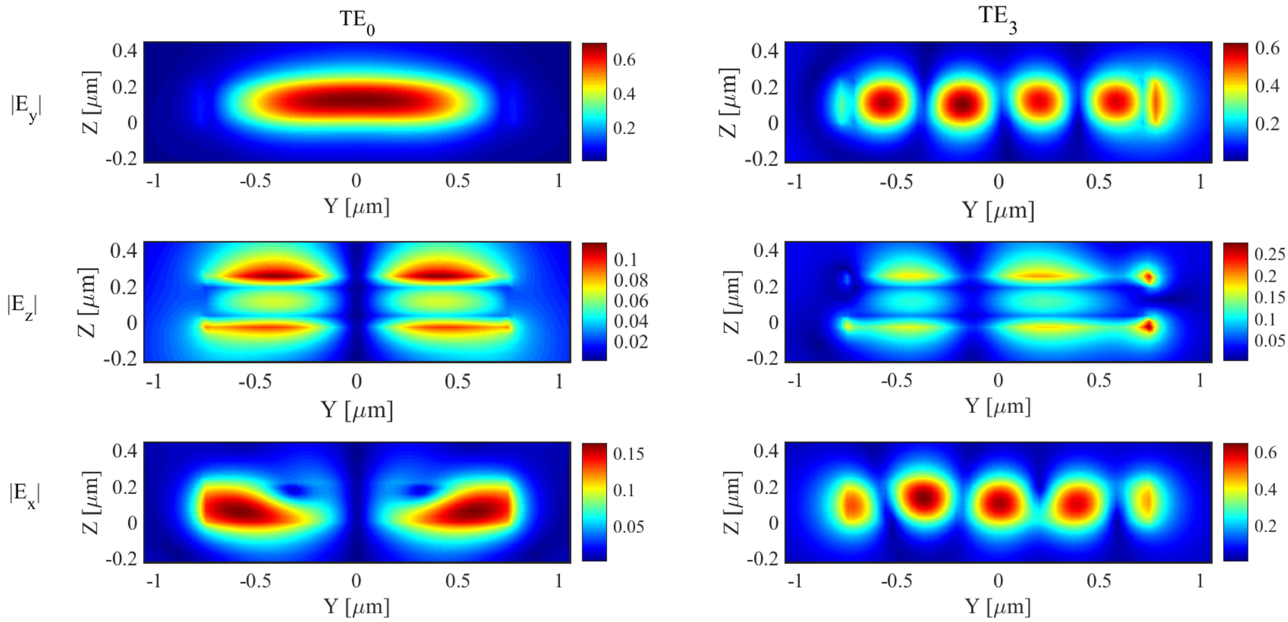

Fig. 7. The output electric field profiles are displayed for TE_0 (first column) and TE_3 (second column) when the input light is TM_1.

the proposed converter has a lower IL by 3 dB approximately. Moreover, noble materials, including gold, are incompatible with CMOS technology [16].

An additional conversion case is introduced to show the eligibility of the proposed structure, by which TM_1 is converted into TE_3 using designed parameters as stated in Table I. This is shown in Fig. 6(b), where IL of -1.5 dB is achieved over a 45 nm bandwidth (between 1528 and 1573 nm) with a device length of 16.937 μm, while maintaining the maximum CT less than -15 dB. It is evident that there is a massive reduction in device length ($\sim 97\,\%$) by analogy with TE_3-to-TM_0 converter reported in [13].

Moreover, it is obvious that spectrum responses generated by both simulation and computational methods, by solving differential coupled equations using MATLAB, are clearly in a good-fit, which confirms the validity of proposed approaches in Sec. IV-A.

The output field components of each conversion are plotted in Fig. 7 to illustrate the spectral analysis. It is observed that the dominant field components of output TE mode, $|E_y|$ and $|E_x|$, are comparable to the similar components of unperturbed TE mode as shown in Fig. 4. However, the weak component of the output TE mode, $|E_z|$, is a portion of the dominant component of the unperturbed input TM mode, $|E_z|$. This observation matches with the monitored maximum CT due to TM_1 displayed in Fig. 6.

C. Fabrication Tolerance Analysis

In this section, performance stability is examined to ensure that it respects the likelihood of fabrication errors. During this part, the mode converter TM_1-to-TE_3 is identified as an example to determine the response towards deviations in grating parameters, including duty cycle τ, etching depth d, period Λ, and waveguide width W, at an operating wavelength of 1550 nm, as depicted in Fig. 8.

It is obvious from Fig. 8(a) that when the duty cycle is chosen to be within the range of 0.6 and 0.7, that is typically ± 20 nm variation, the IL never exceeds -2 dB, whereas CT decreases as the duty cycle goes up within the range mentioned above. In Fig. 8(b), the spectrum response is predicted while changing the etching depth d within the range of ± 20 nm. It is observed that as the etching depth increases, the CT losses become more significant, while the IL does not exceed -2 dB.

When the grating period varies within ± 10 nm, the IL remains almost unchanged at -1.5 dB, but CT decreases with the positive tolerance and *vise versa*, as shown in Fig. 8(c). Since the duty cycle is fixed at 0.65, as the period deviates incrementally, the perturbation strength is relaxed, and the interference ability with unwanted modes decreases. Finally, fabrication variation in waveguide width is analyzed and displayed in Fig. 8(s) with $1400 \leq w \leq 1600$ nm. It is obvious that both IL and CT are almost stable within the variation range of ± 60 nm.

In summary, it can be inferred that the proposed structure shows good fabrication tolerance, and its response is consistent with the coupling analysis performed in Sec. IV-A. It is noteworthy that, the main sources of errors during any fabrication process are due to Electron-Beam Lithography and etching processes. The earlier process puts a constrain on the minimum size that can be implemented. Interestingly, the proposed structure has dimensions that not only exceed the minimum resolution value mentioned in [27], but also have an acceptable margin of deviations. Regarding the etching depth, there is an expected error of < -10 nm compared to what has been reported in [27], which is compatible with the allowable tolerance range of etching grating depth for the proposed structure. Consequently, the practical results would highly match the simulation and computational results.

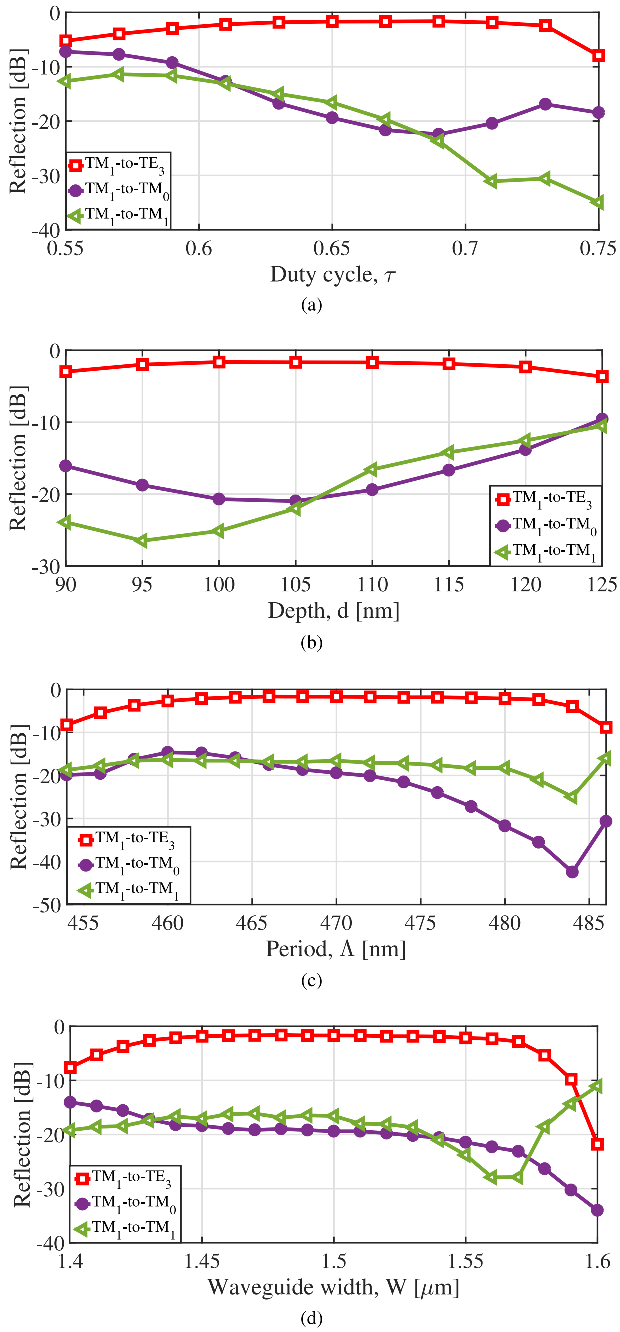

Fig. 8. Fabrication tolerance with deviations of (a) grating duty cycle; (b) etching depth; (c) grating period; and (d) width of the waveguide.

V. Conclusion

An elite periodic structure was introduced through in which coupling among arbitrary modes having different mode orders and polarization states can be accomplished simultaneously. The implication of the proposed structure would open the door to incorporate advanced multiplexing systems in integrated circuits efficiently. Also, coupled-mode equations were reformulated to adapt the presence of engraved grating with oblique plates. The proposed periodic structure was explored by investigating its grating parameters, including tilt angle, duty cycle, and etching depth, to determine the optimum designing values and the available limits for all possible couplings. In addition, the proposed concept was verified by simulating two converters, namely TM_1-to-TE_0 and TM_1-to-TE_3, and both revealed remarkable spectral responses with IL of about -1 and -1.5 dB, with compact lengths of 9.51 and 16.937 μm, respectively. The spectral response was determined using a 3D-FDTD simulation and verified numerically by solving the coupled-mode equations via MATLAB, a good-fit was observed between both responses. Based on these results, the current proposed converter outperformed other related converters reported in previous studies. One of the most remarkable findings is the ability of miniaturizing the converter length while being compatible with CMOS technology. Furthermore, the proposed structure achieved stable performance accompanied with varying grating parameters, including duty cycle, etching depth, period, and width of the strip waveguide. It is worth noticing that rotating the polarization state with the same mode order can be achieved using the same proposed concept.

Acknowledgment

This work is supported by the Ministry of Higher Education and Scientific Research of Egypt.

References

[1] A. Mistry, M. Hammood, S. Lin, L. Chrostowski, and N. A. F. Jaeger, "Effect of lithography on SOI, grating-based devices for sensor and telecommunications applications," in *Proc. IEEE 10th Annu. Inf. Technol., Electron. Mobile Commun. Conf.*, 2019, pp. 0932–0938.

[2] S. TalebiFard *et al.*, "Optimized sensitivity of silicon-on-insulator (SOI) strip waveguide resonator sensor," *Biomed. Opt. Exp.*, vol. 8, no. 2, pp. 500–511, Feb. 2017.

[3] W. Bogaerts and L. Chrostowski, "Silicon photonics circuit design: Methods, tools and challenges," *Laser Photon. Rev.*, vol. 12, no. 4, pp. 1950–1955, Mar. 2018.

[4] C. Li, D. Liu, and D. Dai, "Multimode silicon photonics," *Nanophotonics*, vol. 8, no. 2, pp. 227–247, Feb. 2019.

[5] D. Chen, X. Xiao, L. Wang, Y. Yu, W. Liu, and Q. Yang, "Low-loss and fabrication tolerant silicon mode-order converters based on novel compact tapers," *Opt. Exp.*, vol. 23, no. 9, pp. 11152–11159, May 2015.

[6] H. Wang *et al.*, "Compact silicon waveguide mode converter employing dielectric metasurface structure," *Adv. Opt. Mater.*, vol. 23, no. 9, pp. 1801191-1–1801191-6, Dec. 2019.

[7] Y. Zhao *et al.*, "Ultra-compact silicon mode-order converters based on dielectric slots," *Opt. Lett.*, vol. 45, no. 13, pp. 3797–3800, Jul. 2020.

[8] H. Qiu *et al.*, "Silicon mode multi/demultiplexer based on multimode grating-assisted couplers," *Opt. Exp.*, vol. 21, no. 15, pp. 17904–17911, Jul. 2013.

[9] R. Xiao *et al.*, "On-chip mode converter based on two cascaded Bragg gratings," *Opt. Exp.*, vol. 27, no. 3, pp. 1941–1957, Feb. 2019.

[10] R. Xiao *et al.*, "Integrated Bragg grating filter with reflection light dropped via two mode conversions," *J. Lightw. Technol.*, vol. 37, no. 9, pp. 1946–1953, May 2019.

[11] J. Chen and D. Gao, "Ultra-compact polarization rotator based on mode coupling in a groove-like waveguide, assisted by subwavelength grating," *Appl. Opt.*, vol. 59, no. 18, pp. 5368–5376, Jun. 2020.

[12] H. Okayama, Y. Onawa, D. Shimura, H. Yaegashi, and H. Sasaki, "Polarization rotation Bragg grating using si waveguide with top surface groove grating and terrace," *Japanese J. Appl. Phys.*, vol. 57, no. 4, pp. 042201-1–042201-7, Feb. 2018.

[13] D. Dai, Y. Tang, and J. E. Bowers, "Mode conversion in tapered submicron silicon ridge optical waveguides," *Opt. Exp.*, vol. 20, no. 12, pp. 13425–13439, May 2012.

[14] D. Dai and H. Wu, "Realization of a compact polarization splitter-rotator on silicon," *Opt. Lett.*, vol. 41, no. 10, pp. 2346–2349, May 2016.

[15] Z. Cheng *et al.*, “Broadband and high extinction ratio mode converter using the tapered hybrid plasmonic waveguide,” *IEEE Photon. J.*, vol. 11, no. 3, pp. 1–8, Jun. 2019.

[16] G. V. Naik, V. M. Shalaev, and A. Boltasseva, “Alternative plasmonic materials: Beyond gold and silver,” *Adv. Mater.*, vol. 25, no. 24, pp. 3264–3294, May 2013.

[17] L. Chrostowski and M. Hochberg, *Silicon Photonics Design: From Devices to Systems*. Cambridge, U.K.: Cambridge Univ. Press, Apr. 2015.

[18] E. A. Elzahaby, A. M. R. F. Elbab, and H. Shalaby, “Ultra-compact tunable multi-mode converter based on tilted Bragg gratings in soi waveguides,” in *Proc. IEEE Photon. Soc. Summer Topicals Meeting Ser.*, 2020, pp. 1–4.

[19] E. A. Elzahaby, A. M. R. F. Elbab, and H. Shalaby, “SOI refractive index sensor based on tilted Bragg gratings mode conversion,” in *Proc. 22nd Int. Conf. Transparent Opt. Netw.*, 2020, pp. 1–4.

[20] W. Śmigaj, J. Romero-Vivas, B. Gralak, L. Magdenko, B. Dagens, and M. Vanwolleghem, “Magneto-optical circulator designed for operation in a uniform external magnetic field,” *Opt. Lett.*, vol. 35, no. 4, pp. 568–570, Feb. 2010.

[21] L. Zhu, J. Sun, and Y. Zhou, “Silicon-based wavelength division multiplexer using asymmetric grating-assisted couplers,” *Opt. Exp.*, vol. 27, no. 16, pp. 23234–23249, Aug. 2019.

[22] A. Yariv, “Coupled-mode theory for guided-wave optics,” *IEEE J. Quantum Electron.*, vol. 9, no. 9, pp. 919–933, Sep. 1973.

[23] S. M. Norton, T. Erdogan, and G. M. Morris, “Coupled-mode theory of resonant-grating filters,” *J. Opt. Soc. Amer. A*, vol. 14, no. 3, pp. 629–639, Mar. 1997.

[24] T. Erdogan and J. E. Sipe, “Tilted fiber phase gratings,” *Opt. Lett.*, vol. 13, no. 2, pp. 296–313, Feb. 1989.

[25] K. S. Lee and T. Erdogan, “Fiber mode coupling in transmissive and reflective tilted fiber gratings,” *Appl. Opt.*, vol. 39, no. 9, pp. 296–313, Mar. 2000.

[26] I. Giuntoni *et al.*, “Numerical survey on Bragg reflectors in silicon-on-insulator waveguides,” in *Proc. 5th IEEE Int. Conf. Group IV Photon.*, 2008, pp. 285–287.

[27] R. F. de Cabo, D. González-Andrade, P. Cheben, and A. V. Velasco, “High-performance on-chip silicon beamsplitter based on subwavelength metamaterials for enhanced fabrication tolerance,” *Nanomaterials*, vol. 11, no. 5, pp. 1–11, May 2021.

Eman A. Elzahaby (Member, IEEE) was born in Alexandria, Egypt, in 1989. She received the B.Sc. degree in electronics and communication engineering in June 2010 and the M.Sc. degree in engineering physics in December 2015 from the Faculty of Engineering, Alexandria University, Alexandria, Egypt. Since 2012, she has been with Alexandria University as an Assistant Lecturer. She is currently working toward the Ph.D. degree with the Department of Electronics and Communications Engineering, Egypt-Japan University of Science and Technology (E-JUST). Her research interests include photonic integrated circuits (PICs), silicon photonics, optical fibers, biophotonics and optical sensing.

Ahmed M. R. Fath El Bab received the M.Sc. and Ph.D. degrees from Assiut University, Egypt, in 2002 and 2008, respectively. From October 2006 to October 2008, he was a Visiting Researcher with the Tabata-Lab, Kyoto University, Japan. His research interests include MEMS, tactile sensing, Energy harvesting, and Micro-fluidics. He got the Best Ph.D. Thesis Prize in Engineering, Assiut University, 2010, the prize of Highly Commended paper in Emerald Literati Network, 2017, the Best Paper Award in the IEEE Conference, CIM Sim 2015. He is the Publication Chair of the conference ICIES, 2012, IEEE, RAS. He established the E-JUST Micro-Fabrication CoE. He is a part-time Lecturer with Pan-African University (PAUSTI).

Hossam M. H. Shalaby (Senior Member, IEEE) was born in Giza, Egypt, in 1961. He received the B.S. and M.S. degrees from Alexandria University, Alexandria, Egypt, in 1983 and 1986, respectively, and the Ph.D. degree from the University of Maryland, College Park, United States, in 1991, all in electrical engineering. In 1991, he joined the Electrical Engineering Department with Alexandria University, and was promoted to a Professor in 2001. Since 2017, he has been on leave from Alexandria University, where he is a Professor with the Department of Electronics and Communications Engineering (ECE), School of Electronics, Communications, and Computer Engineering, Egypt-Japan University of Science and Technology (E-JUST), New Borg El-Arab City, Alexandria, Egypt. From 2010 to 2016, he was the Chair of the ECE Department, E-JUST. From December 2000 to 2004, he was an Adjunct Professor with the Faculty of Sciences and Engineering, Department of Electrical and Information Engineering, Laval University, Quebec, QC, Canada. From 1996 to 1998, he was with the Electrical and Computer Engineering Department, International Islamic University Malaysia and from 1998 to 2001, he was with the School of Electrical and Electronic Engineering, Nanyang Technological University, Singapore. He worked as a Consultant with SysDSoft company, Alexandria, Egypt, from 2007 to 2010. His research interests include optical communications, silicon photonics, optical CDMA, and quantum information theory.

Prof. Shalaby has been a Student Branch Counselor of the IEEE E-JUST student branch since 2020. He was a Student Branch Counselor with Alexandria University, IEEE Alexandria, and North Delta Subsection, from 2002 to 2006, and was the Chairman of the Student Activities Committee of IEEE Alexandria Subsection from 1995 to 1996. He received an SRC fellowship from 1987 to 1991 from the Systems Research Center, Maryland, State Excellence Award in Engineering Sciences in 2007 from the Academy of Scientific Research and Technology, Egypt, Shoman Prize for Young Arab Researchers in 2002 from the Abdul Hameed Shoman Foundation, Amman, Jordan, State Incentive Award in Engineering Sciences in 1995 and 2001 from the Academy of Scientific Research and Technology, Egypt, University Excellence Award in 2009 from Alexandria University, and University Incentive Award in 1996 from Alexandria University. He is a Senior Member of the IEEE Photonics Society and The Optical Society (OSA).